



Mechanical and hydraulic properties of fault rocks under multi-stage cyclic loading and unloading

Wentao Hou¹ · Dan Ma^{1,2,3} · Qiang Li¹ · Jixiong Zhang^{1,2,3} · Yong Liu¹ · Chenyao Zhou¹

Received: 31 May 2023 / Revised: 28 July 2023 / Accepted: 3 August 2023
© The Author(s) 2023

Abstract

The rock mass in fault zones is frequently subjected to cyclic loading and unloading during deep resource exploitation and tunnel excavation. Research on the mechanical and hydraulic characteristics of fault rock during the cyclic loading and unloading is of great significance for revealing the formation mechanism of water-conducting pathways in fault and preventing water inrush disasters. In this study, the mechanical and seepage tests of fault rock under the multi-stage cyclic loading and unloading of axial compression were carried out by using the fluid–solid coupling triaxial experimental device. The hysteresis loop of the stress–strain curve, peak strain rate, secant Young's modulus, and permeability of fault rock were obtained, and the evolution law of the dissipated energy of fault rock with the cyclic number of load and unloading was discussed. The experimental results show that with an increase in the cyclic number of loading and unloading, several changes occur. The hysteresis loop of the stress–strain curve of the fault rock shifts towards higher levels of strain. Additionally, both the peak strain rate and the secant Young's modulus of the fault rock increase, resulting in an increase in the secant Young's modulus of the fault rock mass. However, the growth rate of the secant Young's modulus gradually slows down with the increase of cyclic number of loading and unloading. The permeability evolution of fault rock under the multi-stage cyclic loading and unloading of axial compression can be divided into three stages: steady increase stage, cyclic decrease stage, and rapid increase stage. Besides, the calculation model of dissipated energy of fault rock considering the effective stress was established. The calculation results show that the relationship between the dissipated energy of fault rock and the cyclic number of loading and unloading conforms to an exponential function.

Keywords Multi-stage cyclic loading and unloading · Fault rocks · Mechanical properties · Hydraulic properties · Energy dissipation

1 Introduction

The formation of water-conducting pathways in faults is an inherent condition and key factor in the occurrence of water inrush disasters during the process of deep-ground resource exploitation and tunnel excavation (Kang et al. 2010; Wang

et al. 2017). Fault rocks are generated during long-term geological activities and are cemented by highly fractured rock particles (Zhang et al. 2019; Duan et al. 2020b). Due to inadequate cementation and extensive pore development, the mechanical properties and permeability characteristics of fault rock are highly susceptible to stress. At the same time, the fault rock often suffers multi-stage cyclic loading and unloading due to the influence of periodic compression and tectonic stress of roof strata (Tian et al. 2016; Zhao et al. 2019; Yu et al. 2021). Therefore, it is necessary to study the evolution laws of mechanical and hydraulic characteristics during the multi-stage cyclic loading and unloading process of fault rock.

Researchers have conducted extensive research on the mechanical and hydraulic properties of rock masses under multi-stage cyclic loading and unloading (Chen et al. 2007). Song et al. (2022) obtained the mechanical behavior of

✉ Dan Ma
dan.ma@cumt.edu.cn

¹ School of Mines, China University of Mining & Technology, Xuzhou 221116, Jiangsu, China

² State Key Laboratory of Coal Resources & Safe Mining, China University of Mining & Technology, Xuzhou 221116, Jiangsu, China

³ MOE Key Laboratory of Deep Coal Resource Mining, China University of Mining & Technology, Xuzhou 221116, Jiangsu, China

medium-grained sandstone under the horizontal loading and unloading through indoor experiments at the same level, and analyzed the influence of different loading/unloading rates on its mechanical behavior. It was found that when the load level and load path are fixed, the axial strain of the rock in the first and last cycles shows a linear evolution trend, and this linear relationship is independent of the loading/unloading rate. Wang et al. (2022b) conducted horizontal uniaxial cyclic loading and unloading creep tests on rock salt at different loading/unloading rates. The results showed that the axial strain generated by rock salt under uniaxial cyclic loading and unloading mainly occurs in the first cycle; the constant high-pressure results in a significant horizontal section of the rock stress–strain curve, while the constant low pressure has little effect on its stress–strain curve. Ren et al. (2021) investigated the influence of the horizontal cyclic loading at the same level on the coal crushing process. This study reported that the strain accumulation of coal samples gradually increases during the cyclic loading process, and the influence of the first cycle on the microstructure of coal samples is the most significant. Zhang et al. (2018) performed triaxial compression tests on sandstone under different confining pressure loading and unloading rates. It was concluded that the loading and unloading of confining pressure mainly affect the axial strain of sandstone, and there is an exponential function relationship between sandstone permeability and confining pressure. Xue et al. (2017) conducted permeability tests on coal samples under different loading and unloading paths. The study findings suggest that an increase in stress unloading rate leads to a higher susceptibility of coal samples to damage, resulting in increased permeability. However, the previous research failed to consider the mechanical and hydraulic characteristics of fault rock under multi-stage cyclic loading and unloading. Moreover, the physical and mechanical properties of fault rocks differ significantly from those of ordinary rocks. (Jiang et al. 2017; Liang et al. 2019; Wang et al. 2022a, b). Therefore, it is necessary to explore the evolution laws of mechanical and hydraulic characteristics of fault rocks.

In recent years, research on the mechanical and hydraulic properties of fault rock masses has gradually received attention (Hu et al. 2018; Abbasnejadfar et al. 2022; Zhao et al. 2019; Duan et al. 2020a, b). Ferraro et al. (2020) conducted microscopic and ultrasonic tests on fault rocks and found that the petrophysical properties of grain-supported fault rocks and matrix-supported fault rocks were extremely similar, and explored the permeability structure of fault rocks. Wang et al. (2020) analyzed the mechanical properties of matrix supported fault rocks under three stress-loading paths, and analyzed the linear relationship between the uniaxial compressive strength (UCS) variation of cemented paste backfill (CPB) and the instantaneous slope of the stress–strain curve. It was found that the mechanical properties of CPB are

closely related to the setting of stress paths. By investigating the mechanism of fault activation, Graymer et al. (2005) summarized that the properties of individual surrounding rock units (such as rock strength) are crucial factors in determining fault behavior. Odling et al. (2004) combined a three-dimensional statistical model of fault rupture zones with a two-dimensional discrete fault flow model to study the permeability of fault rocks. It was found that after large deformation of fault rocks, its permeability is significantly increased, while the impact of fault sliding on the permeability of fault rocks is relatively low. Through industrial and indoor experiments, Mitchell et al. (2012) predicted the permeability of fault rocks and obtained that as the burial depth of the mine increases, the influence of permeability on fluid flow becomes increasingly significant. The above research indicates that compared to conventional rocks, the mechanical and hydraulic characteristics of fault rocks are significantly different. However, the above research is limited to conventional uniaxial or triaxial mechanical and permeability test tests on fault rock mass. During the coal mining, fault rock is subject to cyclic disturbance of crustal stress (Meng et al. 2022; Zhou et al. 2022). Therefore, it is necessary to study the mechanical and hydraulic characteristics of fault rocks under the multi-stage cyclic loading and unloading of axial compression.

Based on the actual stress environment of fault rock, mechanical and permeability tests on the fault rock under multi-stage loading and unloading were conducted in this study. The hysteresis loop of the stress–strain curve, peak strain rate, secant Young's modulus, and permeability characteristics of the fault rock were obtained, and the evolution law of the dissipated energy of the fault rock with the cyclic number of loading and unloading under different variables was discussed. The research provides a theoretical basis for stable coal mining and groundwater outburst prevention.

2 Experimental methods

2.1 Preparation of samples

Usually, cemented fault rocks are composed of cementitious materials and fractured rocks, while cemented fault rocks generally have low strength and high permeability (Li et al. 2019a; Ma et al. 2021a, b). In this study, The cemented fault rocks were made of water, rock particles, and cementitious agents (Boneh et al. 2014; Dong et al. 2021), among which the rock particles were taken from the fault of the Kekegai Coal Mine in Yulin City, Shaanxi Province, China. Referring to the preparation method proposed by Yin et al. (2018) and Liu et al. (2018), rock samples with physical and mechanical properties similar to fault rocks were prepared using PO42.5

ordinary Portland cement and gypsum as binders. The sample preparation process was as follows:

- (1) Preliminary crushing. A hammer was used to perform preliminary crushing on large-sized rock blocks, as shown in Fig. 1a.
- (2) Secondary crushing. After initial crushing, the small-sized rock blocks were put into a crusher for secondary crushing, as shown in Fig. 1b.
- (3) Rock particle screening. A high-frequency vibration screening machine was used to screen the rock after secondary crushing, and the screened rock particles were classified and stored, as shown in Fig. 1c.
- (4) Slurry preparation. According to Eq. (1), rock particles with different particle sizes, water, Portland cement and gypsum were mixed evenly with a mixer. The sample was prepared using continuously graded rock particles (Ma et al. 2021a, b), and the grading index was 0.5 (Huang et al. 2022). The formula for continuous gradation is as follows:

$$P = (d_m / D_m)^\xi \tag{1}$$

where, P is the mass fraction of rock particles with a particle size smaller than d_m ; d_m is the maximum particle size of one of the three rock particles, mm; D_m is the maximum particle size of all particles, mm; ξ is the grading index.

Table 1 shows the slurry ingredients. The total mass of rock particles in each sample was 640 g, with 369.50 g, 162.06 g, and 108.44 g corresponding to rock particles with the particle size of 0–5 mm, 5–10 mm, and 10–15 mm. The total mass of the binder was 210 g, with a cement-to-gypsum ratio of 2:1. Gypsum was used to delay the cement-setting time and made the fault rock sample more complete. The volume of water was 450 mL.

- (5) Sample preparation. The lubricating oil was applied to the inside of the mold to facilitate subsequent demolding, the evenly stirred slurry was poured into the mold, and the sample to be cured was placed in the curing box, as shown in Fig. 1e. According to a study conducted by Yin et al. (2018), the physical and mechanical properties of the sample are most similar to that of the fault rock when the curing temperature is 20 °C, the curing humidity is 95%, and the curing time is 28 d.

Table 1 Slurry ingredients

Mass of rock particles (g)			Mass of cementing agent (g)	Ratio of cement to gypsum	Volume of water (mL)
0–5 mm	5–10 mm	10–15 mm			
369.50	162.06	108.44	210	2:1	450



Fig. 1 Preparation process for similar materials of weakly cemented fault rocks

Table 2 Basic parameters of samples

Basic parameters	Sample A	Sample B	Sample C
Diameter (mm)	69.81	69.93	69.87
Height (mm)	140.21	140.15	139.91
Density (g/cm^3)	2.56	2.53	2.55
UCS (MPa)	16.25	16.08	16.42
Young's modulus (GPa)	3.42	3.36	3.61
Poisson's ratio	0.18	0.22	0.23
Permeability (μm^2)	1.42	1.53	1.52
Porosity	0.11	0.11	0.11

- (6) Sample completion. After the curing was completed, a demolding machine was used to demould the sample, and the sample preparation was completed, as shown in Fig. 1f. After preparation, samples A, B, and C were selected, and their initial physical and mechanical properties were measured, as shown in Table 2.

2.2 Experimental apparatus

Figure 2 shows the fluid–solid coupling triaxial experimental device for fault rock. This device can accurately control the stress path by using the function of stress gradient loading, and simultaneously realize the simultaneous loading of seepage and stress.

The experimental device consists of an axial pressure control system, a confining pressure control system, a water pressure control system, a simulation room, and a data acquisition system. Figure 3 shows the testing system.

The flow control range of the axial pressure control system and confining pressure control system was 0.0001–70 mL/min, the flow accuracy was 0.0001 mL/min, and the loadable osmotic pressure was 0–70 MPa. The size of the simulated chamber was $\Phi 140\text{mm} \times 220\text{ mm}$, the sample size was $\Phi 70\text{mm} \times 140\text{ mm}$, and the pressure value was 40 MPa.

The main test procedures are as follows:

Step 1: The sample was completely immersed in water for 48 h for saturation. After saturation, the sample was placed in a simulation chamber, and wrapped with a heat shrink sleeve and three circles of electrical tape to tighten the heat shrink sleeve and the sample, ensuring the complete isolation between the sample and the water in the confining pressure chamber.

Step 2: After opening the connecting valve, the axial pressure control system and the confining pressure control system pipeline were connected, and the confining pressure chamber was injected with water under the axial pressure of 0.05 MPa and confining pressure of 1.5 MPa.

Step 3: The water pressure control system was initiated to control the working frequency of the plunger pump, and the stable seepage pressure was kept.

Step 4: The loading path was set according to the test plan in Table 4, and multi-stage loading and unloading tests were conducted.

Step 5: After the experiment was completed, the test data were collected.

2.3 Stress paths and experimental program

In this study, the loading upper limit, loading time, unloading time and seepage pressure were selected as test variables. The confining pressure of each group of samples

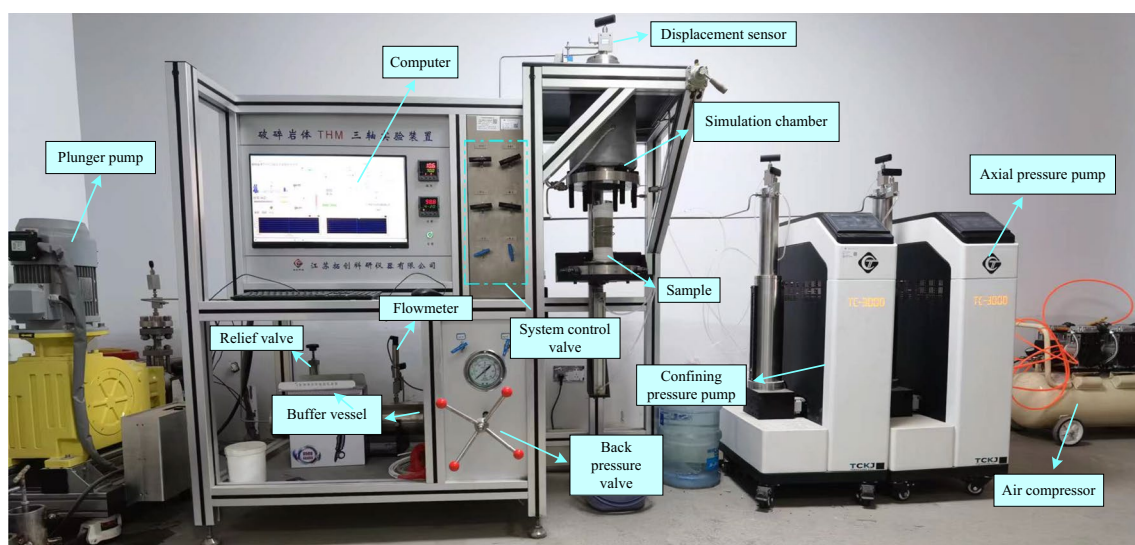


Fig. 2 Triaxial experimental apparatus of fault rocks under mechanical-hydraulic coupling

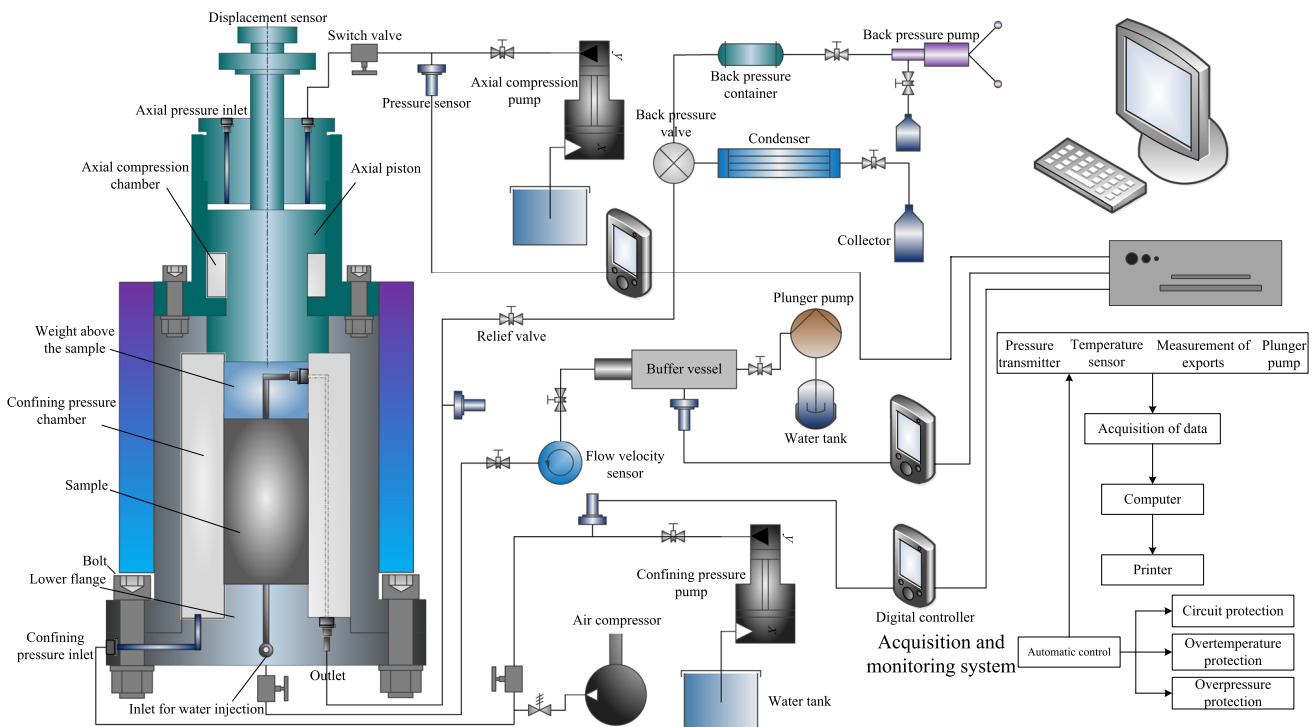


Fig. 3 Experimental system

Table 3 Test plan for multi-stage cyclic loading and unloading of fault rock

Sample number	Stress path (MPa)	Loading time (min)	Unloading time (min)	Seepage pressure (MPa)
1	4-3-8-3-12-3-16-3-20-0	10	3	2
2	4-3-7-3-10-3-13-3-16-0			
3	4-3-9-3-14-3-19-3-24-0			
4	4-3-8-3-12-3-16-3-20-0	8	3	2
5		12		
6	4-3-8-3-12-3-16-3-20-0	10	2	2
7			4	
8	4-3-8-3-12-3-16-3-20-0	10	3	1.5
9				2.5

during the test was 1.5 MPa. Table 3 shows the specific test scheme.

Figure 4 shows the loading path set for this experiment. The five cycles of axial loading and unloading were performed for each group of tests, and the upper limit of axial compression was incrementally increased, while the lower limit of unloading remained unchanged at 3 MPa, and the loading and unloading rate of axial pressure is 5 MPa/s.

Sample 1 was the control sample. For Sample 1, the initial axial pressure was 4 MPa, the upper limit of axial compression was incrementally increased by 4 MPa, the loading time was 10 min, the unloading time was 3 min, and the seepage pressure was 2 MPa.

To study the influence of the upper limit of axial compression, the upper limit of axial compression of Sample 2 and Sample 3 was incrementally increased by 3 MPa and 5 MPa, and the other parameters (loading time, unloading time and seepage pressure) were same as those of Sample 1.

To investigate the effect of loading time, the loading time of Sample 4 and Sample 5 was set as 8 min and 12 min, and the remaining parameters were the same as those of Sample 1.

To investigate the effect of unloading time, the unloading time of Sample 6 and Sample 7 was 2 min and 4 min, and the remaining parameters were the same as those of Sample 1.

To study the influence of seepage pressure, the seepage pressures of Sample 8 and Sample 9 were set as 1.5 MPa and 2.5 MPa, and the remaining parameters were the same as those of Sample 1.

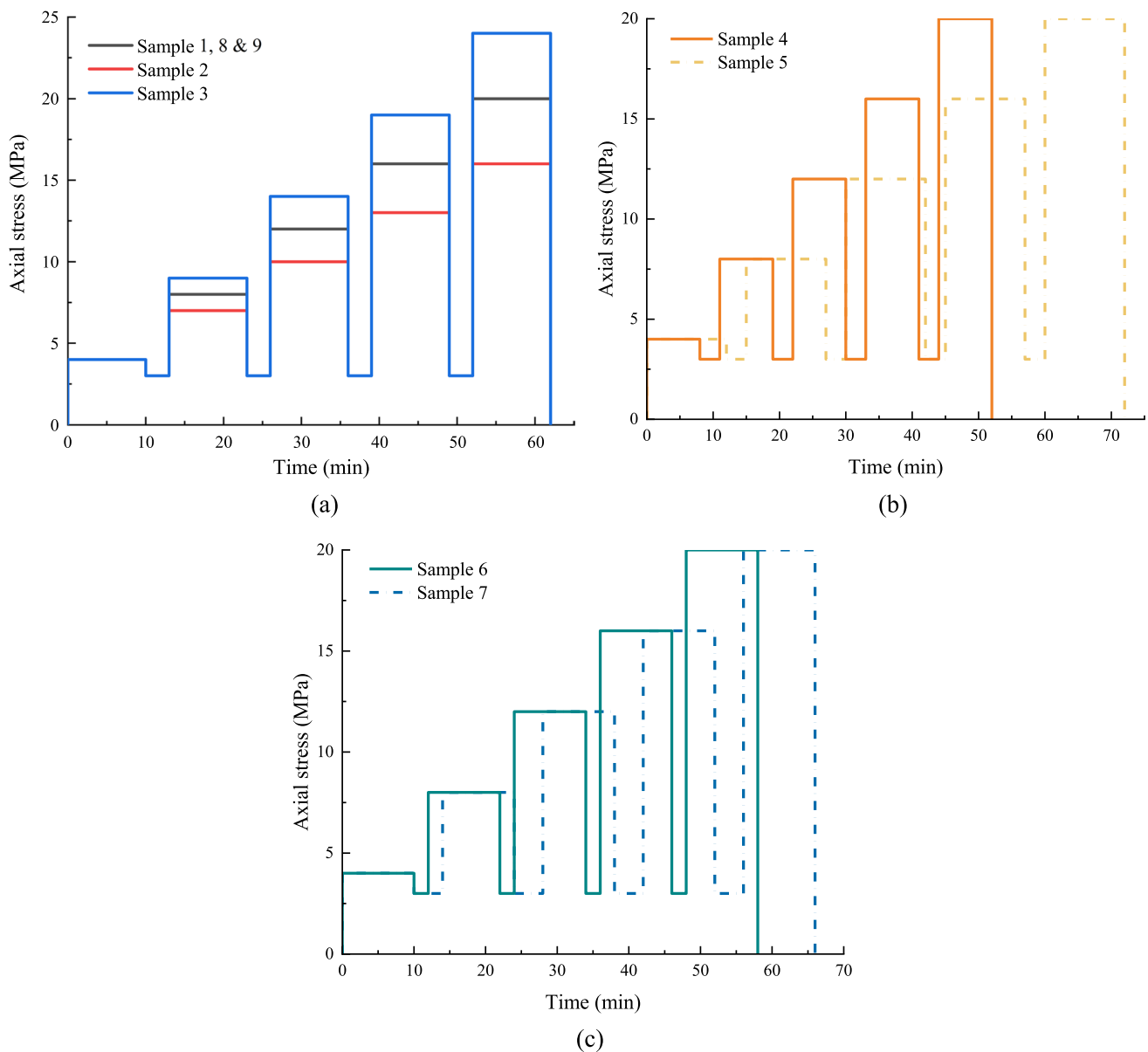


Fig. 4 Stress paths setting. **a** Samples 1, 2, 3, 8 and 9; **b** Samples 4 and 5; **c** Samples 6 and 7

3 Experimental results

3.1 Stress–strain behaviors

3.1.1 Basic characteristics of the stress–strain hysteresis loops

Figure 5 shows the stress–strain curves of fault rocks under different experimental variables. It can be seen that the stress–strain curve of the fault rock exhibits a hysteresis loop regardless of variations in testing conditions. During the cyclic loading stage, there are some microcracks and

pores inside the compacted sample under axial compression. After the compaction, some of the microcracks and pores cannot be restored during the unloading stage, resulting in residual strain in the sample. Due to the presence of residual strain, the cyclic loading curve and unloading curve cannot completely overlap, and the loading curve always sits above the unloading curve, forming a plastic hysteresis loop.

It is worth noting that as the number of cyclic loading and unloading increases, the hysteresis loop shifts towards higher levels of strain and undergoes a transition from densification to dilation. This phenomenon exhibits the same characteristics in Figs. 5a–d. During the cycling loading and

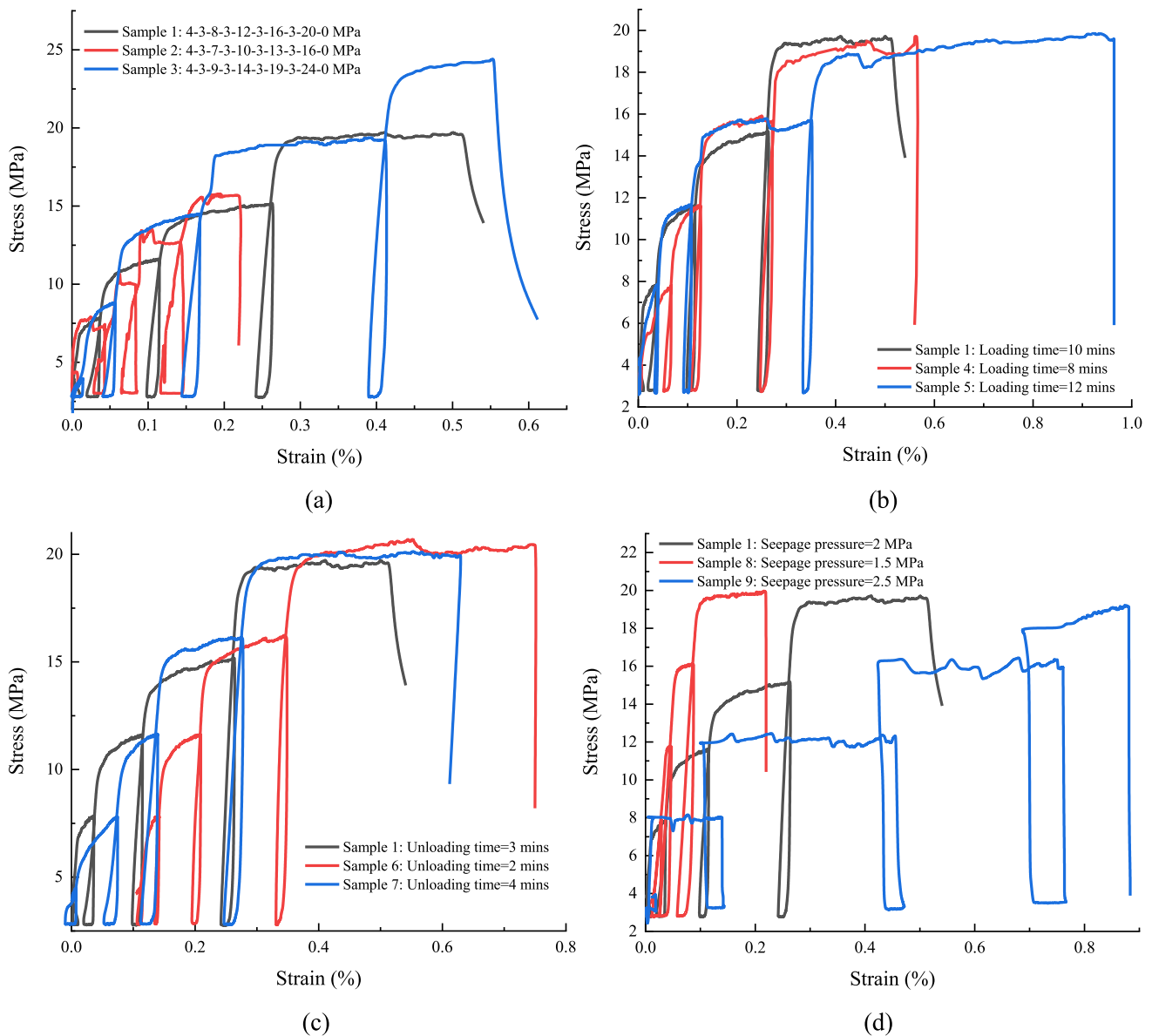


Fig. 5 Stress–strain curves of fault rocks under different variables. **a** Upper limit of axial compression; **b** Loading time of axial compression; **c** Unloading time of axial compression; **d** Seepage pressure

unloading process, as the upper limit of axial compression continuously increases, the secondary cracks inside the sample gradually increase, and the residual strain of the sample gradually increases, causing the hysteresis loop to gradually move towards the higher levels of strain. The hysteresis loop varying from dense to sparse indicates that as the cyclic number increases, the sample generates greater strain, and the strain of the sample reaches a stable or accelerated creep stage.

Figure 5a shows the stress–strain curve of fault rock with the upper limit of axial compression as the variable. It can be observed that the strain increase of the same sample mainly occurs during the 3rd, 4th, and 5th loading. After

the one, two, three and four cycles and the fifth loading, the strain of the Sample 3 is 0.0024×10^{-3} , 0.0052×10^{-3} , 0.1632×10^{-3} , 0.4028×10^{-3} and 0.5512×10^{-3} , respectively. This is because the stress in the first cycle is relatively low, and the sample is in the compaction stage. The original cracks and pores inside the sample are compacted, resulting in smaller deformation of the sample. As the upper limit of axial compression continues to increase, the sample generates more secondary cracks during the loading stage, and the deformation of the sample rapidly increases.

As shown in Fig. 5a, as the upper limit of axial compression increases, the hysteresis loop of the stress–strain curve of the sample moves to the right of the horizontal

axis under the same cycle. After four cycles, the hysteresis loops of Samples 2, 1, and 3 are located on the horizontal axis of 0.1402×10^{-3} , 0.2502×10^{-3} , 0.4028×10^{-3} , respectively. It can be inferred that as the upper limit of axial compression increases, the sample enters the accelerated creep strain stage earlier, and the damage amount of the sample increases, and the hysteresis loop shifts to the right side of the horizontal axis.

Figure 5b shows the stress–strain curves of Samples 1, 4, and 5 under multi-stage cyclic loading and unloading. During the first three cycles, there is no significant relationship between the position of the hysteresis loop on the abscissa axis of the stress–strain curve of the sample and the loading time. During the fourth cycle, the position of the hysteresis loop does not change significantly for samples with shorter loading time (8 min, 10 min). When the loading time increases to 12 min (Sample 5), the hysteresis loop moves significantly to the right side of the horizontal axis. After the four cycles, the horizontal coordinates of the hysteresis loops of Samples 4, 1, and 5 are 0.2489×10^{-3} , 0.2502×10^{-3} and 0.3325×10^{-3} , respectively. It can be inferred that the sample is in the initial creep strain stage due to the lower upper limit of axial compression during the first three cycles, and its strain increases over time with a slow rate of increase. At the fourth cycle, due to the short loading time, Samples 1 and 4 are still in the initial creep strain stage, while Sample 5 enters the stable creep strain stage due to the longest loading time. At this time, the strain of sample 5 significantly increases, and the hysteresis loop moves towards the right side of the horizontal axis.

Figure 5c shows the stress–strain curves of Samples 1, 6, and 7 under different unloading time. It can be seen that the sample with the shortest unloading time (2 min) has the highest strain, and with the extension of unloading time (3 mins, 4 mins), there is a small strain change in the sample. After the four cycles, the hysteresis loops of Samples 6, 1, and 7 are located at abscissa positions of 0.3285×10^{-3} , 0.2502×10^{-3} and 0.2593×10^{-3} , respectively. This is because the elastic strain generated by the sample during the loading stage recovers during the unloading stage. The longer the unloading time, the more complete the elastic strain recovery of the sample. In the fourth cyclic unloading stage, the unloading time of sample 6 is the shortest, and the elastic strain recovery of the sample is incomplete, and the strain of sample 6 is the largest; while the unloading time of Samples 1 and 7 is longer, and the elastic strain recovery is complete. Therefore, the strain changes of the two groups of samples are not significant.

Figure 5d shows the stress–strain curves of Samples 1, 8 and 9 under the different seepage pressures. It can be found that the an increase in seepage pressure causes a rightward shift of the hysteresis loop in the stress–strain curve of the sample. After the four cycles, the hysteresis loops

of Samples 8, 1, and 9 are located at abscissa positions of 0.0792×10^{-3} , 0.2502×10^{-3} and 0.7825×10^{-3} , respectively. The rock particles within the sample undergo migration as a result of water seepage behavior. The higher the water pressure, the more severe the particle loss inside the sample, and the greater the damage and deformation of the sample. Consequently, the hysteresis loop of the stress–strain curve of the sample shifts towards the right side of the horizontal axis.

3.1.2 Peak strain rate

The multi-stage triaxial loading and unloading test of variable strain loading rate shows that the change in strain rate can reflect the strength and deformation characteristics of rock mass (Si et al. 2019; Wang et al. 2021). This study also investigates the peak strain rate characteristics of fault rock under multi-stage cyclic loading and unloading, as shown in Fig. 6.

As the upper limit of axial compression increases, the peak strain rate of the sample increases, as shown in Fig. 6a. For example, during the fifth loading, the peak strain rates of Sample 2, Sample 1, and Sample 3 are $1.04 \times 10^{-5}/s$, $1.42 \times 10^{-5}/s$ and $1.62 \times 10^{-5}/s$, respectively. After the fifth unloading, the elastic strain generated by the sample during the loading stage is basically restored. However, due to the incremental loading method, the sample is subjected to a higher upper limit of axial compression during the loading stage of the next cycle, then the strain rapidly increases and the peak strain rate increases. It is worth noting that during the fifth cycle, the strain of the sample increases sharply. It can be inferred that due to the largest upper limit of axial compression at this time, the sample enters the accelerated creep strain stage, and the peak strain rate of the sample suddenly increases, ultimately leading to the sample failure.

Figure 6b shows the bar graph of the peak strain rate of the fault rock under different loading time. It can be seen that the peak strain rate of the sample decreases with the extension of loading time. During the third cycle, the peak strain rates of Samples 4, 1, and 5 were $8.54 \times 10^{-6}/s$, $7.56 \times 10^{-6}/s$, $5.27 \times 10^{-6}/s$, respectively. The extension of loading time results in more residual strains generated during the creep process of the sample. In the creep process, more residual strain is generated, resulting in less strain in the next cycle.

The extension of unloading time increases the peak strain rate of the sample, as shown in Fig. 6c. During the fifth cycle, the peak strain rates of Samples 6, 1, and 7 are $6.49 \times 10^{-6}/s$, $1.42 \times 10^{-5}/s$ and $1.76 \times 10^{-5}/s$, respectively. This is because the unloading time is extended, and the elastic strain of the sample generated in the previous cycle is recovered effectively. After the loading stage of the fifth cycle, the strain generated by the sample increases, leading to an increase in the peak strain rate of the sample.

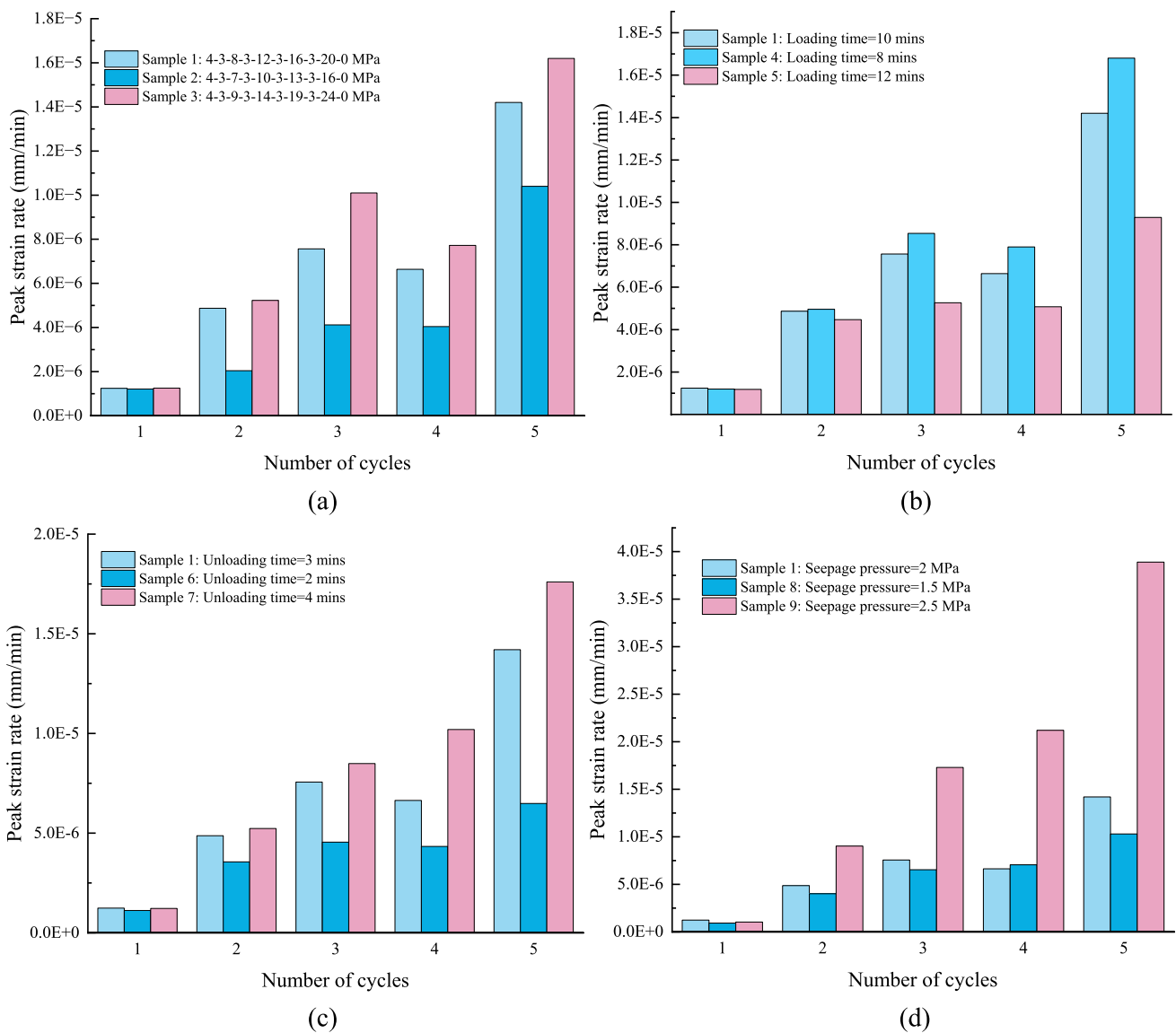


Fig. 6 Histogram of peak strain rate of fault rock under multi-stage cyclic loading and unloading

The strain rate of deep underground rock mass changes constantly due to the seepage effect of aquifer water. In this experiment, the evolution process of the peak strain rate of fault rock under the synchronous action of stress seepage is also studied. The experimental results are shown in Fig. 6d. When the seepage pressure increases from 1.5 MPa (sample 8) to 2 MPa (sample 1), the peak strain rate of the sample has no significant change. When the seepage pressure increases to 2.5 MPa (sample 9), the peak strain rate of the sample increases significantly. For example, the peak strain rate of specimen 9 reaches $3.89 \times 10^{-5}/s$ during the fifth cycle, which is obviously higher than the peak strain rate of all other samples in each cycle. It indicates that the seepage pressure is the main controlling factor of the peak strain rate of fault rock. In this test, the erosion effect of water pressure

of 1.5 MPa and 2 MPa on the rock particles in the sample is not obvious. When the seepage pressure increases to 2.5 MPa, the seepage behavior of water induces significant migration of rock particles in the sample, the integrity of the sample is destroyed, the deformation resistance is weakened, and the peak strain rate of the sample increases sharply.

3.1.3 Secant Young's modulus

The secant Young's modulus can reflect the deformation resistance of the sample at a certain moment. It is an important parameter for studying the strength evolution of fault rocks affected by mining disturbances. Figure 7 shows the evolution curves of the Young's modulus of the fault rock

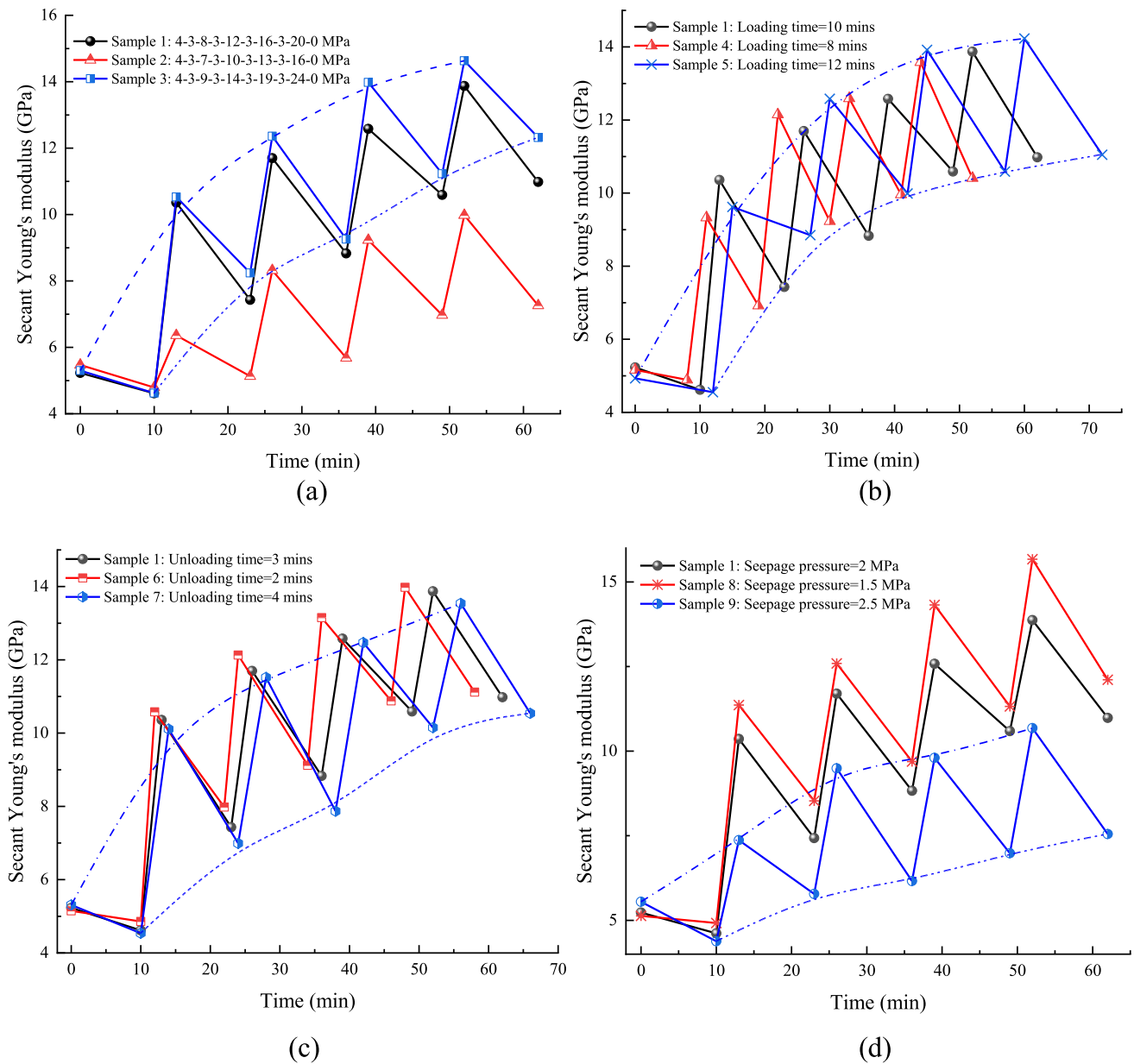


Fig. 7 Time-varying curve of Young's modulus of fault rock under multi-stage cyclic loading and unloading

under multi-stage cyclic loading and unloading. It can be found that the secant Young's modulus of fault rock exhibits similar evolutionary characteristics under different variables.

(1) During each cycle, the secant Young's modulus of the sample increases with time at the loading stage. This indicates that the pores of the sample are continuously compressed during the loading period, and the sample's resistance to deformation is enhanced. Conversely, the secant Young's modulus of the sample decreases with time at the unloading stage, indicating that the recov-

ery of elastic strain leads to a decrease in the sample's resistance to deformation.

- (2) As the cyclic number increases, the upper limit of the secant Young's of the sample increase continuously, as well as the lower limit of the secant Young's modulus at the unloading stage. This indicates that multi-stage cyclic loading and unloading can enhance the strength of the sample.
- (3) The loading method of multi-stage cyclic loading and unloading can improve the deformation resistance of the sample; as the cyclic number increases, the growth

rate of the peak and valley values of Young's modulus of the sample gradually slows down during each cycle, indicating that there is a threshold value for the enhanced strength of the sample. When the secant modulus of the sample approaches the threshold, the secant Young's modulus will not increase or even decrease due to the failure of the sample.

Figure 7a shows the evolution curve of the Young's modulus of the fault rock with the upper limit of axial compression as a variable. During the same cycle, with the increase in the upper limit of axial compression, both the peak value of the secant Young's modulus of the sample during the loading stage and the valley value of the secant Young's modulus during the unloading stage increase. For instance, during the third cycle, the peak values of the secant Young's modulus of Samples 2, 1, and 3 during the loading stage are 9.23 GPa, 12.58 GPa, and 13.98 GPa, respectively; while the valley values of the secant Young's modulus during the unloading stage are 6.97, 10.59, and 11.23 GPa, respectively. Due to the increase in the upper limit of axial compression, the internal cracks of the sample become more closed during the loading stage, the deformation resistance of the sample is enhanced, and the peak value of the secant Young's modulus of the sample during the loading process increases. As some cracks in the specimen are compacted in the loading stage, more residual strain is generated in the specimen, and the valley value of the secant line Young's modulus of the specimen increases in the unloading stage.

Figure 7b shows the time-dependent curve of the secant Young's modulus of the specimen affected by loading time. Due to different loading time, the secant Young's modulus of the sample exhibits irregular changes. It can be inferred that under a short loading time (8–12 min in this experiment), the secant Young's modulus of the sample does not change with the change of loading time.

The test results show that the secant Young's modulus of the sample is free from the short loading time in this experiment. Interestingly, the effect of unloading time on the secant Young's modulus of the sample is very significant, as shown in Fig. 7c. As the unloading time increases, the peak and valley values of the secant Young's modulus of the sample decrease during the loading stage and unloading stage. During the third cycle, the peak values of the secant Young's modulus of Samples 6, 1, and 7 during the loading stage are 13.15 GPa, 12.58 GPa, and 12.47 GPa, respectively. The valley values of the secant Young's modulus during the unloading stage are 10.88, 10.59, and 10.15 GPa, respectively. Due to the same upper limit of axial compression and loading time, the residual strain generated during the loading process of the sample is similar. As the unloading time prolongs, the elastic strain recovery of the sample increases,

the deformation resistance of the sample weakens, and the secant Young's modulus decreases.

Figure 7d shows the time-varying curve of Young's modulus of secant of fault rock under different seepage pressures. It can be seen that the secant Young's modulus of the sample at the same time decreases as the seepage pressure increases in the same cycle. When loaded to 30 min, the secant Young's moduli of Samples 8, 1, and 9 are 11.73 GPa, 10.46 GPa, and 7.94 GPa, respectively. It can be speculated that the seepage behavior of water can reduce the deformation resistance of the sample. The higher the seepage pressure, the more serious the particle loss inside the sample, and the smaller the secant Young's modulus of the sample.

3.2 Hydraulic properties

Compared to conventional rock permeability tests, it is difficult to explore the evolution law of hydraulic characteristics of fault rocks under multi-stage cyclic loading and unloading. To analyze the hydraulic properties of fault rock, the permeability of the rock is examined in this study. Accurately obtaining the evolution law of the permeability of fault rock is of great significance for preventing and controlling mine water inrush caused by fault-connected underground aquifers (Ma et al. 2017; Sun et al. 2022).

Figure 8 presents the time-varying permeability characteristics of fault rocks under multi-stage cyclic loading and unloading. During the first four cycles, the permeability of the sample continuously decreases during loading and continuously increases during unloading. This can be explained as follows. During the loading process, the internal cracks of the sample are closed under external forces, leading to a decrease in permeability. During the unloading process, the elastic strain of the sample recovers, and some cracks reopen, resulting in an increase in permeability.

Although the experimental variables are different, the permeability time-varying curves of all samples can be divided into three evolution stages:

- (1) **Steady increase stage:** This stage occurs during the first cycle. During the first loading, the permeability of the sample slowly decreases, and during the first unloading, the permeability of the sample rapidly increases, reaching the maximum permeability in the first four cycles. Due to the lowest upper limit of axial compression in the first cycle, the plastic deformation of the sample is the smallest, and the work done by external forces is mainly converted into the accumulated elastic strain of the sample. When the loading is completed, the elastic strain of the sample begins to recover, and the permeability continues to increase.

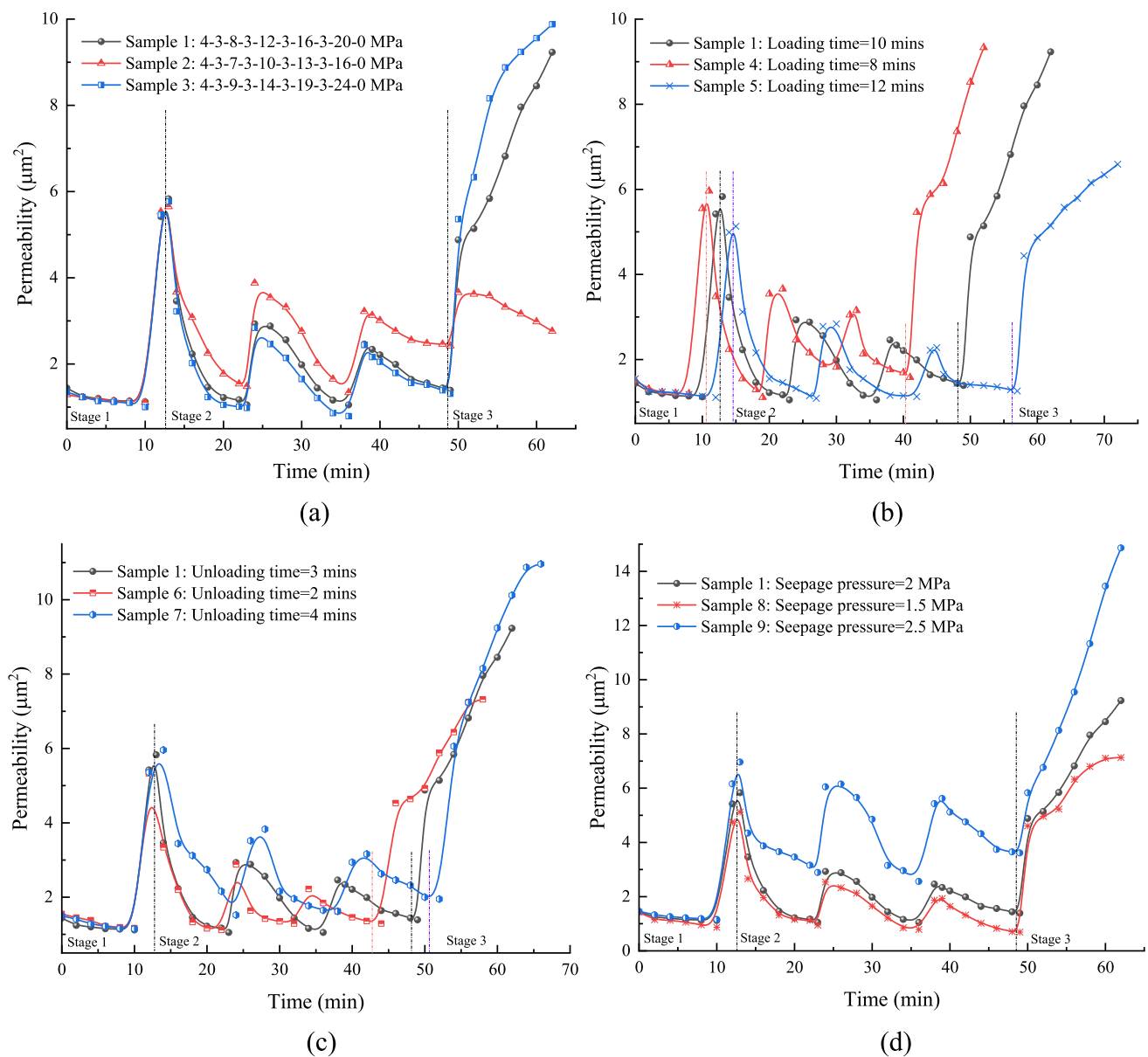


Fig. 8 Time-varying properties of permeability of fault rocks under different variables. **a** Upper limit of axial compression; **b** Loading time of axial compression; **c** Unloading time of axial compression; **d** Seepage pressure

- (2) **Cyclic decrease stage.** This stage mainly occurs from the beginning of the second loading to the end of the fourth loading. At this stage, the permeability of the sample shows a "wave-like" downward trend as the cyclic number increases. As the cyclic number increases, the upper limit of axial compression increases, and the cumulative plastic strain of the sample increases. Even if the sample is unloaded, the peak permeability of the sample cannot exceed the peak permeability of the previous cycle.
- (3) **Rapid increase stage.** This stage mainly occurs from the beginning of the fourth unloading to the end of the fifth loading. In this stage, the permeability of the sample increases rapidly, reaching the maximum permeability throughout the entire cycle. Due to the upper limit of the axial compression during the fifth loading, the sample is damaged, the internal cracks of the sample are gradually interconnected, and the water-conducting pathways are formed. As a result, the permeability of

the sample rapidly increases. This stage is also a stage prone to water inrush in engineering practice.

The increase or decrease in the upper limit of axial compression can significantly affect the time-varying characteristics of specimen permeability, as shown in Fig. 8a. As the upper limit of axial compression increases, the permeability of the sample decreases during the steady increase stage and cyclic decrease stages, and increases during the rapid increase stage. After a 30-min test, the permeability of Samples 2, 1, and 3 is $2.76 \mu\text{m}^2$, $1.98 \mu\text{m}^2$, $1.65 \mu\text{m}^2$, respectively. After a 60-min test, the permeability of Samples 2, 1, and 3 is $2.98 \mu\text{m}^2$, $8.45 \mu\text{m}^2$, $9.56 \mu\text{m}^2$, respectively. In the increase stage and cyclic decrease stage, the inadequate stress at this time cannot result in the sample failure, and the upper limit of axial compression increases, contributing to a denser interior of the sample, narrower water-conducting pathways and lower permeability. In the rapid increase stage, the upper limit of axial compression for Samples 1 and 3 is 20 MPa and 24 MPa, respectively. At this time, the loading and unloading effect of the high-graded axial compression leads to sample failure, the internal cracks of the sample are connected, the number of water-conducting pathways increases, and the sample permeability increases rapidly. As the maximum axial compression is 16 MPa, sample failure does not occur, and the permeability of Sample 2 during the fifth cycle is still in the cyclic decrease stage.

The permeability time-varying curve of fault rock under multi-stage cyclic loading and unloading under different loading time is obtained, as shown in Fig. 8b. As the loading time prolongs, the permeability of the sample decreases at the end of unloading during the first four cycles. As the loading time prolongs, the creep time of the sample increases, and the interior of the sample becomes denser, resulting in a decrease in permeability.

As the unloading time prolongs, the permeability of the sample increases at the end of the unloading of the first four cycles, as shown in Fig. 8c. At the end of the unloading of the second cycle, the permeability of Samples 6, 1, and 7 is $2.88 \mu\text{m}^2$, $2.93 \mu\text{m}^2$ and $3.83 \mu\text{m}^2$, respectively. When the unloading time is prolonged, the elastic strain recovery of the sample is more complete, the internal pores of the sample are opened, and the sample permeability increases.

Figure 8d shows the time-varying characteristic curve of the permeability of the sample under different seepage pressures. When the seepage pressure increases from 1.5 to 2 MPa, the permeability of the sample at the same time increases slightly. When the seepage pressure increases to 2.5 MPa, the permeability of sample 9 increases significantly. After the 30-min test, the permeability of Samples 8, 1, and 9 is $1.65 \mu\text{m}^2$, $1.98 \mu\text{m}^2$ and $4.85 \mu\text{m}^2$, respectively. With the increase of seepage

pressure, the erosion effect of water seepage on the rock particles inside the sample is enhanced, the water-conducting pathway inside the sample is widened, and the permeability is increased. When the seepage pressure is 2.5 MPa, the erosion effect of water seepage is particularly strong, and the permeability of the sample is significantly increased.

4 Discussion

4.1 The improved model for dissipated energy of the rock mass

According to the laws of energy conversion and conservation, the failure of fault rocks is an unstable phenomenon driven by energy (Liu et al. 2020). Under the influence of cyclic loads caused by coal mining, fault rocks receive, store, and release energy due to their own energy characteristics. Energy dissipation causes damage to the rock, leading to lithology degradation and strength loss (Xie et al. 2005a, 2005b). With the increasing depth of coal mining, the energy state of fault rock undergoes continuous changes, resulting in a gradual evolution of internal cracks from small to macroscopic through-cracks. When the energy state of fault rock becomes unstable, the integrated large cracks in the rock cause rock failure. Analyzing the energy changes of rock mass during multi-stage loading and unloading from an energy perspective can better explain the mechanical characteristics of deep-fault rock under the influence of coal mining.

In traditional methods, the area of the hysteresis loop curve is usually used to represent the dissipated energy of the sample. In practical engineering, rock mass is not only affected by axial stress, but also by radial stress and water pressure, contributing to the energy instability of the rock mass. Therefore, the concept of effective stress is introduced to enhance the accuracy of the dissipated energy calculation for rock masses.

In the loading and unloading process of fault rock, the input mechanical energy is converted into elastic strain energy stored in the rock and dissipated energy released during rock failure (Li et al. 2019a, b; Peng et al. 2019; Kong et al. 2022). According to the law of conservation of energy:

$$W = E_e + U_d \quad (2)$$

where, W is the total energy input by external forces, J ; E_e is the elastic potential energy, J ; U_d is the dissipated energy, J .

In this experiment, the total energy W input by external forces is the work done by the testing machine on the sample, which can be calculated by Eq. (3) as follows:

$$W = \int \sigma_1 d\varepsilon_1 + \int \sigma_2 d\varepsilon_2 + \int \sigma_3 d\varepsilon_3 \quad (3)$$

where, σ_1 is the axial stress, MPa; ε_1 is axial strain. In this experiment, the sample is a cylindrical body and subjected to isotropic confining pressure. Therefore, $\sigma_2 = \sigma_3 = \sigma_c$, is the radial stress, MPa. Equation (3) can be converted as follows:

$$W = \int \sigma_1 d\varepsilon_1 + 2 \int \sigma_c d\varepsilon_c \quad (4)$$

The elastic potential energy E_e can be calculated by Eq. (5).

$$E_e = E_{e1} + E_{e2} + E_{e3} \quad (5)$$

where E_{ei} is the elastic energy generated by each principal strain, J.

The elastic energy generated by the specimen under anisotropic strain is as follows:

$$E_{ei} = \sigma_i \varepsilon_i \quad (6)$$

According to the generalized Hooke's law, the stress–strain law of rocks satisfies the following relationship:

$$\varepsilon_1 = \frac{\sigma_1 - \bar{\mu}_1(\sigma_2 + \sigma_3)}{\bar{E}_1} \quad (7)$$

$$\varepsilon_2 = \frac{\sigma_2 - \bar{\mu}_2(\sigma_1 + \sigma_3)}{\bar{E}_2} \quad (8)$$

$$\varepsilon_3 = \frac{\sigma_3 - \bar{\mu}_3(\sigma_1 + \sigma_2)}{\bar{E}_3} \quad (9)$$

where, \bar{E}_i is the average Young's modulus in each direction of the sample during the multi-stage cyclic loading and unloading process, MPa; $\bar{\mu}_i$ is the average Poisson's ratio in all directions.

Assuming that the sample is an isotropic material, then

$$\bar{E}_1 = \bar{E}_2 = \bar{E}_3 = \bar{E} \quad (10)$$

$$\bar{\mu}_1 = \bar{\mu}_2 = \bar{\mu}_3 = \bar{\mu} \quad (11)$$

By combining Eqs. (7) and (11) and bringing them into Eq. (6), it can be obtained that:

$$E_{ei} = \frac{\sigma_i^2 - \bar{\mu} \sigma_i (\sigma_j + \sigma_k)}{\bar{E}} \quad (12)$$

Considering that the specimen is a cylindrical body and subjected to equal radial stresses, Eq. (13) can be obtained by incorporating Eq. (12) into Eq. (5):

$$E_e = \frac{\sigma_c^2(3 - 2\bar{\mu}) - 4\bar{\mu}\sigma_1\sigma_c}{\bar{E}} \quad (13)$$

In this experiment, in addition to elastic energy produced by multi-stage cyclic loading and unloading and confining pressure, the sample is also subjected to water pressure, resulting in changes in elastic and dissipated energy. Therefore, the concept of effective stress is introduced, and Eq. (13) can be expressed by:

$$E_e = \frac{\sigma_h^2(3 - 2\bar{\mu}) - 4\bar{\mu}\sigma_v\sigma_h}{\bar{E}} \quad (14)$$

where, σ_v is the axial support force between rock particles, i.e. the effective axial stress, MPa; σ_h is the radial effective stress, MPa.

According to the principle of force balance, Eq. (15) can be obtained:

$$\sigma_1 S = \sigma_v(1 - \phi)S + p\phi S \quad (15)$$

where, S is the area of the horizontal cross-section of the sample, m^2 ; ϕ is the porosity of the rock mass; p is the seepage pressure, MPa.

Equation (15) is converted into an expression for the axial effective stress equation as follows:

$$\sigma_v = \frac{\sigma_1 - p\phi}{1 - \phi} \quad (16)$$

Similarly, by selecting the longitudinal section of the specimen as the research object, the radial effective stress expression of the specimen can be obtained:

$$\sigma_h = \frac{\sigma_c - p\phi}{1 - \phi} \quad (17)$$

By introducing Eqs. (16) and (17) into Eq. (14), the calculation principle of rock elastic energy considering effective stress can be obtained:

$$E_e = \frac{(\sigma_c - p\phi)^2(3 - 2\bar{\mu}) - 4\bar{\mu}(\sigma_c - p\phi)(\sigma_1 - p\phi)}{(1 - \phi)^2 \bar{E}} \quad (18)$$

By combining Eqs. (2), (5), and (18), the calculation equation for dissipated energy considering effective stress can be obtained:

$$U_d = \int \sigma_1 d\varepsilon_1 + 2 \int \sigma_c d\varepsilon_c - \frac{(\sigma_c - p\phi)^2(3 - 2\bar{\mu}) - 4\bar{\mu}(\sigma_c - p\phi)(\sigma_1 - p\phi)}{(1 - \phi)^2 \bar{E}} \quad (19)$$

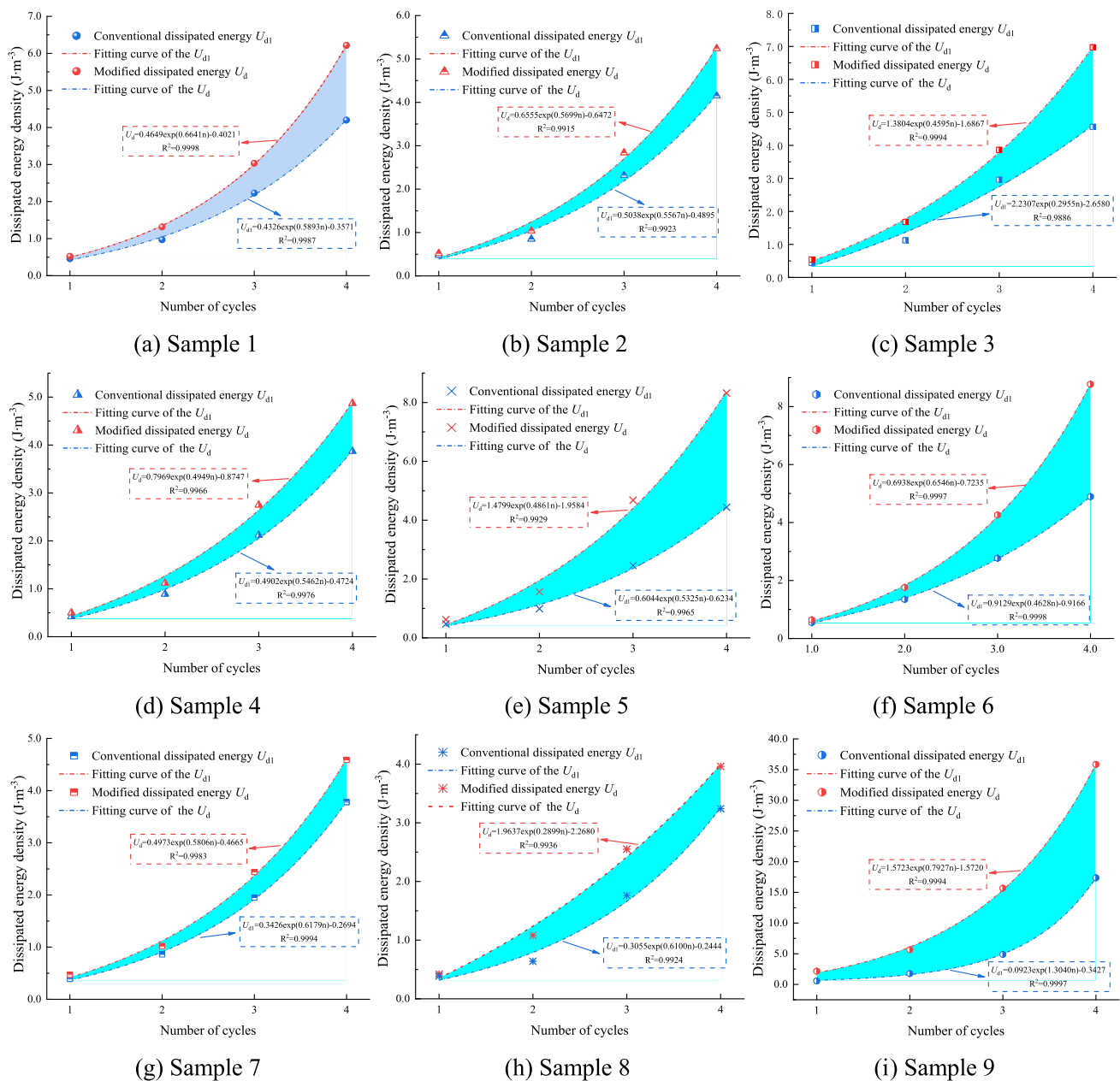


Fig. 9 Dissipated energy of fault rock and its fitting curve before and after modification

4.2 Analysis of rock energy dissipation under multi-stage cyclic loading and unloading

The unit dissipated energy provides a more precise means of comparing and analyzing the impact of various factors on the energy characteristics of rock masses. The dissipated energy calculated by traditional methods and improved methods for nine groups of samples are statistically analyzed. The dissipated energy is plotted in the form of dissipated energy density, and the dissipated energy calculated by the two methods is fitted, as shown in Fig. 9. The shaded area in

the figure represents the deviation of dissipated energy after considering effective stress, and Table 4 displays the cumulative dissipated energy and discrepancies before and after improvement.

As shown in Figs. 9a–i, the dissipated energy of the sample exhibits an exponential relationship with cyclic number. The dissipated energy of the sample calculated by the improved method is always greater than that by traditional methods. With the increase of the cyclic number, the dissipated energy of the sample calculated by the traditional method and the improved method increase, and

Table 4 Cumulative dissipated energy before and after modification

Sample group	Cumulative conventional dissipated energy density (J/m ³)	Cumulative modified dissipated energy density (J/m ³)	Dissipated energy density deviation (J/m ³)
Sample 1	1.59	2.68	1.09
Sample 2	1.51	1.98	0.47
Sample 3	0.94	2.16	1.22
Sample 4	1.38	1.60	0.22
Sample 5	1.55	2.80	1.25
Sample 6	1.47	3.78	2.31
Sample 7	1.50	1.74	0.24
Sample 8	0.78	1.27	0.49
Sample 9	13.24	18.53	5.29

their deviation also increases. Since the seepage pressure is considered in the effective stress, the water seepage can accelerate the damage of the sample, leading to an increase in the dissipated energy. Therefore, the dissipated energy of the sample obtained by the improved method is always greater than the that by traditional method. In the first two cycles, the work done by the testing machine on the sample is mainly used for the accumulation of elastic potential energy of the sample, and the sample is less damaged. The dissipated energy obtained by the traditional method is close to that by the improved method. As the cyclic number continues to increase, the accumulated amount of elastic potential energy of the sample reaches the threshold, and the accumulated amount of dissipated energy of the sample increases. At this time, the number of cracks in the sample increases, and the seepage pressure accelerates the loss of rock particles in the sample; the seepage pressure further increases the dissipated energy of the sample, and the deviation between the dissipated energy calculated by the traditional method and the improved method increases.

As shown in Figs. 9a–c, with the increase in the upper limit of axial compression during the same cycle, the improved dissipated energy of the specimen increases. As for the third cycle, the improved dissipated energy of sample 2 (10 MPa), sample 1 (12 MPa), and sample 3 (14 MPa) are 2.84 J/m³, 3.03 J/m³ and 3.86 J/m³, respectively. As the upper limit of axial compression increases, the input energy of the testing machine to the sample increases. This results in a higher probability of instability and failure within the sample, leading to an increase in dissipated energy. As listed in Table 4, as the upper limit of axial compression increases, the deviation of dissipated energy accumulation obtained by the improved method and the traditional method increases. The deviation of the dissipated energy accumulation in Samples 2, 1, and 3 is 0.47 J/m³, 1.09 J/m³ and 1.22 J/m³ respectively. This is because the high stress causes serious damage to the sample, intensifies the particle migration effect of seepage pressure, promotes the accumulation of dissipated

energy of the sample, and leads to an increase in the deviation of dissipated energy.

The calculation curves of sample dissipated energy in Figs. 9a, d, and e indicate that extending the loading time can increase the dissipated energy of the sample calculated by the improved method during the same cycle. For example, in the third cycle, the dissipated energy of sample 4 (8 min), sample 1 (10 min), and sample 5 (12 min) calculated by the improved method are 2.75 J/m³, 3.03 J/m³, 4.68 J/m³, respectively. As the working time of the testing machine increases on the sample, the accumulated elastic potential energy of the sample can reach the threshold quickly, and the external input energy begins to transform into dissipated energy, leading to an increase in dissipated energy. Referring to Table 4, as the loading time prolongs, the deviation of accumulated dissipated energy calculated by the improved method and the traditional method increases. When the loading time is prolonged, the sample is damaged in advance, the water-conducting pathway inside the sample is widened, and the input work of the seepage pressure on the sample increases, leading to the increase of the accumulated dissipated energy of the sample.

As shown in Figs. 9a, f, and g, the dissipated energy of the sample calculated by the improved method decreases with the extension of unloading time under the same cycle. Taking the fourth cycle as an example, the improved dissipated energy of sample 6 (2 min) is 8.77 J/m³, while the improved dissipated energy of sample 7 (4 min) is only 4.59 J/m³. Because the elastic potential energy accumulated in the loading stage partially escapes in the unloading stage, the sample needs to continue to accumulate the elastic potential energy at the next cycle, resulting in a decrease in the dissipated energy of the sample. Similarly, the deviation of dissipated energy of the sample also decreases with the extension of unloading time, such as the deviation of dissipated energy of sample 7 being only 0.24 J/m³. With the increase of unloading time, the escape of dissipated elastic potential energy of

the sample increases, the dissipated energy for expanding the internal fracture network of the sample is insufficient. Consequently, the seepage channel inside the sample narrows, and the work done by the seepage pressure decreases, leading to a decrease in the deviation of dissipated energy.

As shown in Figs. 9a, h and i, the seepage pressure is the main controlling factor for the evolution of the dissipated energy of the sample, and the dissipated energy of the sample increases significantly with the increase of the seepage pressure. In the fourth cycle, the dissipated energy of sample 8 (1.5 MPa) and sample 9 after the improvement is 3.96 J/m³ and 35.84 J/m³. With the increase of seepage pressure, the total work input from the outside increases, and the improved dissipated energy of the sample increases. As shown in Table 4, with the increase of seepage pressure,

the deviation between the dissipated energy calculated by the improved method and the traditional method increases.

4.3 Evolution mechanism of rock dissipated energy under multi-stage cyclic loading and unloading

The energy dissipation of rocks originates from the transformation of numerous small energy storage structures inside the rocks into dissipation structures. Figure 10 demonstrates the evolution mechanism of dissipated energy of rock materials under multi-stage cyclic loading and unloading conditions. Before the generation and diffusion of microcracks inside the rock, the total work input by external forces on the rock is transformed into elastic potential energy. The increase in elastic potential energy leads to denser internal

Fig. 10 Evolution mechanism of dissipated energy under multi-stage cyclic loading and unloading

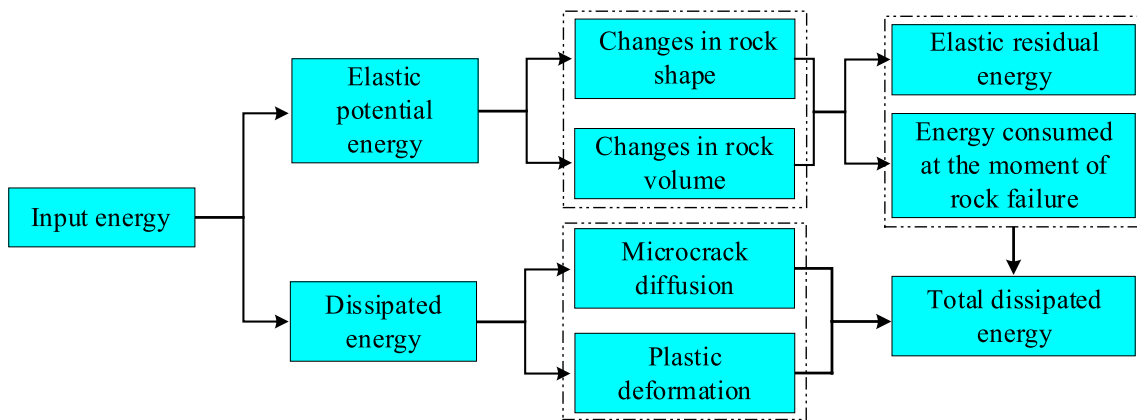
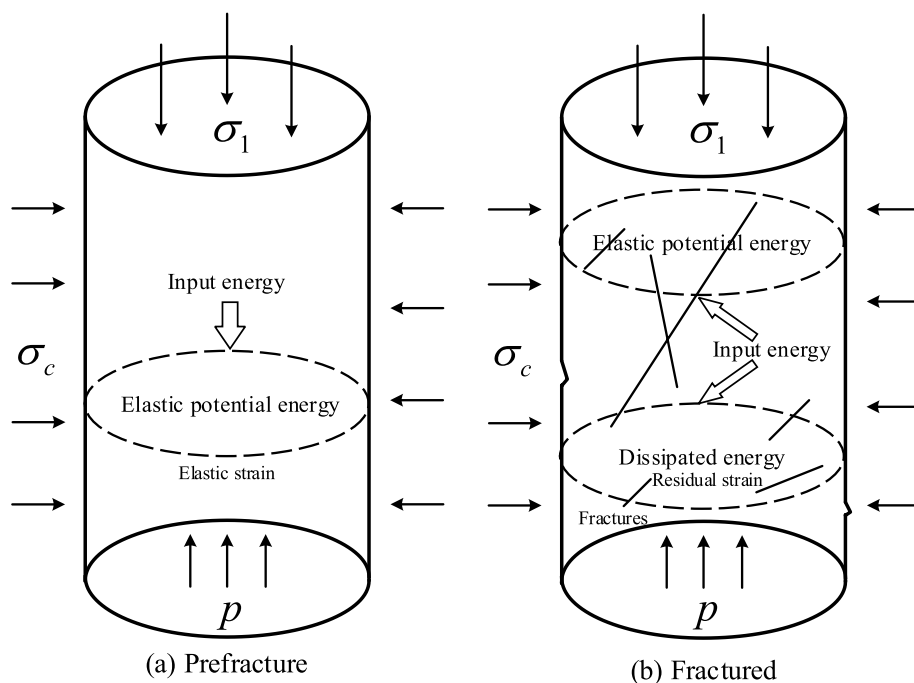


Fig. 11 Rock energy distribution architecture

microcracks and an increase in rock strength. After unloading, the elastic potential energy accumulated by the rock is released accompanied by volume expansion and structural relaxation, resulting in a decrease in physical and mechanical properties. When a higher axial compression is applied to the rock again, the elastic potential energy of the rock becomes saturated, and the work input by external forces begins to be converted into dissipated energy. The development and expansion of rock cracks are more complete, and the higher the cyclic stress level, the greater the accumulation of dissipated energy in the rock, until the rock failure occurs.

Figure 11 shows the energy distribution structure of rocks after external forces input work. According to the law of energy conservation, the work done by external forces on rocks is divided into elastic potential energy and dissipated energy without considering heat exchange. The energy required for changes in rock shape and volume belongs to elastic potential energy. After rock failure, some of the elastic potential energy is consumed at the moment of rock failure, while the remaining elastic potential energy is stored in the form of elastic residual energy inside the rock. The energy required for the generation of microcracks and plastic deformation of rocks during loading belongs to dissipated energy, and the greater the dissipated energy, the more severe the rock fracture.

5 Conclusions

To reveal the formation mechanism of the water-conducting pathway in the fault rock during deep ground resource exploitation and tunnel excavation, mechanical and seepage tests on fault rock under the multi-stage cyclic loading and unloading of axial compression were conducted, and the evolution law of the dissipated energy of fault rock with the cyclic number was studied under different variables. The main conclusions are as follows:

- (1) As the upper limit of axial compression increases, the hysteresis loop of the stress-strain curve moves to the right of the horizontal axis; as the loading time increases, the strain of the specimen significantly increases; As the unloading time increases, the recovery amount of elastic strain the sample increases; With the increase of seepage pressure, the hysteresis loop of the stress-strain curve shifts to the right of the abscissa axis.
- (2) The peak strain rate of the fault rock increases with the increase of the cyclic number of loading and unloading. As the upper limit of axial compression increases, the peak strain rate of the sample increases under the same cycle; The extension of loading time results in

a decrease in the peak strain rate of the sample; The extension of unloading time results in an increase in the peak strain rate of the sample; When the seepage pressure of the sample is low (e.g., 1.5 MPa, 2 MPa), the peak strain rate of the sample is less affected by the seepage pressure. When the seepage pressure increases to 2.5 MPa, the peak strain rate of the sample increases significantly.

- (3) The secant Young's modulus of rock mass under multi-stage cyclic loading and unloading increases with the increase of the cyclic number, but its growth rate gradually slows down. As the upper limit of axial compression increases, the peak value of the secant Young's modulus during the loading stage and the valley value of the secant Young's modulus during the unloading stage of the sample also increase; The secant Young's modulus of the sample is less affected by the loading time; As the unloading time increases, the secant Young's modulus of the sample decreases; With the increase of seepage pressure, the secant Young's modulus of the sample at the same stage decreases.
- (4) Under the multi-stage cyclic loading and unloading, the permeability time-varying curve of the sample can be divided into three evolution stages: steady increase stage, cyclic decrease stage, and rapid increase stage. With the increase in the upper limit of axial compression, the permeability of the sample in the first two stages significantly reduces; The extension of loading time leads to a decrease in the permeability of the sample; The permeability of the sample increases with the increase of seepage pressure with the extension of unloading time.
- (5) Considering the influence of effective stress and pore pressure, an improved energy dissipation model for fault rock was established. The results indicate that the dissipated energy of fault rock under cyclic loading and unloading conditions increases exponentially with the number of loading and unloading cycles. The dissipated energy of fault rock is positively correlated with the upper limit of axial compression, the loading time and the seepage pressure, and negatively correlated with the unloading time.

Acknowledgements This study was supported by the National Science Fund for Excellent Young researchers of Science China (52122404), the National Natural Science Foundation of China (41977238).

Author contributions WH: Formal analysis, Conceptualization, Methodology, Writing Original Draft. DM: Funding Acquisition, Supervision, Project Administration, Conceptualization. QL: Methodology, Writing—Review and Editing, Validation. JZ: Writing—Review and Editing, Methodology, Supervision. YL: Methodology, Software. CZ: Software.

Availability of data and materials The data and materials used to support the findings of this study are included within the article.

Declarations

Competing interest The authors declare that the research was conducted in the absence of any commercial or financial relationships that could be construed as a potential conflict of interest.

Open Access This article is licensed under a Creative Commons Attribution 4.0 International License, which permits use, sharing, adaptation, distribution and reproduction in any medium or format, as long as you give appropriate credit to the original author(s) and the source, provide a link to the Creative Commons licence, and indicate if changes were made. The images or other third party material in this article are included in the article's Creative Commons licence, unless indicated otherwise in a credit line to the material. If material is not included in the article's Creative Commons licence and your intended use is not permitted by statutory regulation or exceeds the permitted use, you will need to obtain permission directly from the copyright holder. To view a copy of this licence, visit <http://creativecommons.org/licenses/by/4.0/>.

References

- Abbasnejadfar M, Bastami M, Hashemi SA (2022) Experimental investigation on the stress-strain behavior of unsaturated polyester polymer concrete subjected to monotonic and cyclic loadings. *J Build Eng* 48:103966
- Boneh Y, Chang JC, Lockner DA, Reches Z (2014) Evolution of wear and friction along experimental faults. *Pure Appl Geophys* 171:3125–3141
- Chen YP, Wang SJ, Wang EZ (2007) Strength and elastic properties of sandstone under different testing conditions. *J Cent South Univ* 14:210–215
- Dong FX, Peng Z, Sun WB, Zhou SL, Kong LJ (2021) Experimental research on the effect of water-rock interaction in filling media of fault structure. *Geomech Eng* 24(5):471–478
- Duan MK, Jiang CB, Gan Q, Li MH, Peng K, Zhang WZ (2020a) Experimental investigation on the permeability, acoustic emission and energy dissipation of coal under tiered cyclic unloading. *J Nat Gas Sci Eng* 73:103054
- Duan MK, Jiang CB, Gan Q, Zhao HB, Yang Y, Li ZK (2020b) Study on permeability anisotropy of bedded coal under true triaxial stress and its application. *Transport Porous Med* 131:1007–1035
- Ferraro F, Agosta F, Prasad M, Vinciguerra S, Violay M, Giorgioni M (2020) Pore space properties in carbonate fault rocks of peninsular Italy. *J Struct Geol* 130:103913
- Graymer RW, Ponce DA, Jachens RC, Simpson RW, Phelps GA, Wentworth CM (2005) Three-dimensional geologic map of the Hayward fault, northern California: correlation of rock units with variations in seismicity, creep rate, and fault dip. *Geology* 33(6):521–524
- Hu XB, Lu QW, Xu ZH, Zhang WL, Cheng SS (2018) Compressive stress-strain relation of recycled aggregate concrete under cyclic loading. *Constr Build Mater* 193:72–83
- Huang CF, Zhang SL, Gao YT, Wu SC, Zhou Y, Sun H, Wang WQ, Wang Y, Yang WZ (2022) Triaxial permeability test of fault fractured tuff based on Talbot theory. *J Cent South Univ* 53(8):3092–3103
- Jiang CB, Duan MK, Yin GZ, Wang JG, Lu TY, Xu J, Zhang DM, Huang G (2017) Experimental study on seepage properties, AE characteristics and energy dissipation of coal under tiered cyclic loading. *Eng Geol* 221:114–123
- Kang H, Zhang X, Si L, Wu Y, Gao F (2010) In-situ stress measurements and stress distribution characteristics in underground coal mines in China. *Eng Geol* 116:333–345
- Kong LW, Xie HP, Gao C, Li CB (2022) Experimental and theoretical research on the anisotropic deformation and energy evolution characteristics of shale under uniaxial cyclic loading and unloading. *Int J Geomech* 22(11):04022208
- Li SC, Wu J, Xu ZH, Yang WM (2019a) Mechanics criterion of water inrush from the coal floor under influence of fault and its engineering application. *Int J Geomech* 19:04019022
- Li TT, Pei XJ, Wang DP, Huang RQ, Tang H (2019b) Nonlinear behavior and damage model for fractured rock under cyclic loading based on energy dissipation principle. *Eng Fract Mech* 206:330–341
- Liang DX, Zhang N, Xie LX, Zhao GM, Qian DY (2019) Damage and fractal evolution trends of sandstones under constant-amplitude and tiered cyclic loading and unloading based on acoustic emission. *Int J Distrib Sens N* 15:1550147719861020
- Liu C, Li SC, Zhou ZQ, Li LP, Wang K, Hou FJ, Qin CS, Gao CL (2018) Model test on mechanical characteristics of surrounding rock during construction process of super-large section tunnel in complex strata. *Rock Soil Mech* 39(9):3495–3504
- Liu XH, Hao QJ, Hu AK, Zheng Y (2020) Study on determination of uniaxial characteristic stress of coal rock under quasi-static strain rate. *Chin J Rock Mech Eng* 39(10):2038–2046
- Ma D, Rezaia M, Yu HS, Bai HB (2017) Variations of hydraulic properties of granular sandstones during water inrush: Effect of small particle migration. *Eng Geol* 217:61–70
- Ma D, Duan HY, Zhang JX, Feng XJ, Huang YL (2021a) Experimental investigation of creep-erosion coupling mechanical properties of water inrush hazards in fault fracture rock masses. *Chin J Rock Mech Eng* 40(9):1751–1763
- Ma D, Zhang JX, Duan HY, Huang YL, Li M, Sun Q, Zhou N (2021b) Reutilization of gangue wastes in underground backfilling mining: overburden aquifer protection. *Chemosphere* 264:128400
- Meng F, Pu H, Dintwe TKM, Sasaoka T, Xu J (2022) Creep and breakage behavior of broken rock in the caved zone of abundant mines under triaxial compression condition. *Energy Rep* 8:14517–14532
- Mitchell TM, Faulkner DR (2012) Towards quantifying the matrix permeability of fault damage zones in low porosity rocks. *Earth Planet Sc Lett* 339:24–31
- Odling NE, Harris SD, Knipe R (2004) Permeability scaling properties of fault damage zones in siliclastic rocks. *J Struct Geol* 26(9):1727–1747
- Peng K, Wang YQ, Zou QL, Liu ZP, Mou JH (2019) Effect of crack angles on energy characteristics of sandstones under a complex stress path. *Eng Fract Mech* 218:106577
- Ren QQ, Zhang YF, Arauzo I, Shan LY, Xu J, Wang Y, Su S, Hu S, Xiang J (2021) Roles of moisture and cyclic loading in microstructures and their effects on mechanical properties for typical Chinese bituminous coals. *Fuel* 293:120408
- Si XF, Gong FQ, Li XB, Wang SY, Luo S (2019) Dynamic Mohr-Coulomb and Hoek-Brown strength criteria of sandstone at high strain rates. *Int J Rock Mech Min* 115:48–59
- Song ZY, Konietzky H, Wu YF, Du K, Cai X (2022) Mechanical behaviour of medium-grained sandstones exposed to differential cyclic loading with distinct loading and unloading rates. *J Rock Mech Geotech Eng* 14:1849–1871
- Sun DD, Hou XA, Yang TH, Zhao Y, Zhang PH, Yang B, Liu YL, Ma K (2022) Calibration of water inrush channel and numerical simulation of water inrush process in coal mine roof. *Front Earth Sci* 10:931508
- Tian WL, Yang SQ, Fang G (2016) Particle flow simulation on mechanical behavior of coal specimen under triaxial cyclic loading and unloading. *J China Coal Soc* 41(3):603–610

- Wang HL, Xu WY, Cai M, Xiang ZP, Kong Q (2017) Gas permeability and porosity evolution of a porous sandstone under repeated loading and unloading conditions. *Rock Mech Rock Eng* 50:2071–2083
- Wang J, Fu JX, Song WD (2020) Mechanical properties and microstructure of layered cemented paste backfill under triaxial cyclic loading and unloading. *Constr Build Mater* 257:119540
- Wang XH, Huang XF, Gao MN, Zhao YP (2021) Mechanical response of kerogen at high strain rates. *Int J Impact Eng* 155:103905
- Wang G, Feng XT, Yang C, Han Q, Kong R (2022a) Experimental study of the mechanical characteristics of jinping marble under multi-stage true triaxial compression testing. *Rock Mech Rock Eng* 55:953–966
- Wang JB, Zhang Q, Liu X, Song ZP, Feng SJ (2022b) Creep properties and constitutive model for salt rock subjected to uniaxial trapezoidal cyclic loading. *J Energy Storage* 52:105023
- Xie HP, Ju Y, Li LY (2005a) Criteria for strength and structural failure of rocks based on energy dissipation and energy release principles. *Chin J Rock Mech Eng* 24(17):3003–3010
- Xie HP, Peng RD, Ju Y, Zhou HW (2005b) On energy analysis of rock failure. *Chin J Rock Mech Eng* 24(15):2603–2608
- Xue Y, Ranjith PG, Gao F, Zhang D, Cheng H, Chong Z, Hou P (2017) Mechanical behaviour and permeability evolution of gas-containing coal from unloading confining pressure tests. *J Nat Gas Sci Eng* 40:336–346
- Yin Q, Jing HW, Su HJ, Zhao HH (2018) Experimental study on mechanical properties and anchorage performances of rock mass in the fault fracture zone. *Int J Geomech* 18(7):04018067
- Yu HD, Chen WZ, Gong Z, Tan XJ, Yang DS (2021) Loading-unloading behavior of a clayey rock under thermo-hydro-mechanical conditions. *Int J Rock Mech Min* 148:104966
- Zhang C, Zhang L (2019) Permeability characteristics of broken coal and rock under cyclic loading and unloading. *Nat Resour Res* 28:1055–1069
- Zhang DM, Yang YS, Chu YP, Zhang X, Xue YG (2018) Influence of loading and unloading velocity of confining pressure on strength and permeability characteristics of crystalline sandstone. *Res Phys* 9:1363–1370
- Zhao YR, Yang HQ, Huang LP, Chen R, Chen XS, Liu SY (2019) Mechanical behavior of intact completely decomposed granite soils along multi-stage loading-unloading path. *Eng Geol* 260:105242
- Zhou JX, Zhang JW, Wang JA, Li F, Zhou Y (2022) Research on nonlinear damage hardening creep model of soft surrounding rock under the stress of deep coal resources mining. *Energy Rep* 8:1493–1507

Publisher's Note Springer Nature remains neutral with regard to jurisdictional claims in published maps and institutional affiliations.